Estimating acoustic radiation from a Bernoulli–Euler beam using shaped polyvinylidene flouride film

Brian L. Scott
Graduate Program in Acoustics, The Pennsylvania State University, University Park, Pennsylvania 16802

Scott D. Sommerfeldt
Department of Physics and Astronomy, Brigham Young University, Provo, Utah 84602

(Received 3 July 1996; accepted for publication 8 February 1997)

This paper examines numerically the use of arrayed shaped polyvinylidene fluoride film sensors to obtain an estimate of the far-field radiated power from a clamped-clamped Bernoulli–Euler beam excited by a sinusoidal point force. Distributed sensors are designed that are sensitive to the radiated power. Fourier analysis of point and distributed sensor outputs is used to estimate the beam's radiated power. The numerical results of the estimated power obtained from the point and distributed sensors are compared to those predicted by the theoretical model and the performance of the two sensor types is assessed. The results show that the shaped sensors provide a reasonable estimate of the strain transforms over the region of interest, when compared to the exact theoretical predictions, for the first five beam resonance frequencies and for frequencies located approximately midway between resonance frequencies. The distributed sensors also give consistently better predictions of the strain transforms for all frequencies considered when compared to the point sensor results. The power predictions using shaped sensors range from -1 to 3 dB relative to the exact theoretical results for most of the frequencies analyzed. This contrasts to the 36–68 dB range of relative power estimates using point sensors. [S0001-4966(97)02606-4]

PACS numbers: 43.40.Rj, 43.38.Fx [CBB]

INTRODUCTION

A number of methods exist to obtain the acoustic radiation from a vibrating structure. Examples include an analytical model of the structure to predict radiated power, microphones to perform far-field or intensity measurements, or accelerometers to obtain the structure's vibrational response. A known model assumption has the benefit of not requiring additional financial, weight, or space costs, but normally cannot model the structure completely and lacks the ability to adapt to changes in the system. Using transducers to collect real-time data allows the prediction of radiated power even when system parameters change. If transducers are used, the physical quantity to be measured and the location of the sensors are important considerations.

The radiation from a structure can be determined by placing transducers away from the structure, as is the case when using microphones to record the pressure levels in the surrounding fluid. Unattached sensors have the benefit of having little or no effect on the behavior of the system under consideration and measure only what is radiated when implemented properly. However, locating transducers off the structure is often not suitable due to environmental constraints. Mounting sensors directly on the structure, for instance by using accelerometers, can solve this problem. In addition, this type of sensor is not influenced by secondary pathways and might be better for implementing active control of the structure. Since the desire is to determine the radiated power, transducers that are sensitive to radiation, not simply vibration, are required. One possibility for achieving this is to use distributed sensors mounted to the structure.

Using distributed sensors allows the fabrication of sensors that are sensitive to specific vibrational characteristics of the structure. Work done by Burke on a pinned beam illustrates the use of shaping polyvinylidene fluoride (PVDF) film, a piezoelectric material, in terms of singularity functions to design a sensor that is sensitive to the beam's velocity or moment at a specific location.[1] Burke demonstrated how a sensor with a given width at one end of the beam that decreases linearly to zero at the other end is sensitive to the beam's moment at the tip with the nonzero film width. Burke has also extended this work to two-dimensional systems.[2] Weighting functions that produce sensors that are sensitive to the modal vibration of a structure were demonstrated by Lee and Moon.[3] Other shape functions and their benefits are discussed in Refs. 4–6. These works are significant in that they discuss the use of shape functions and windows to achieve frequency or wave number roll-off with distributed sensors.

Discrete sensors can also be used to obtain wave number information. Maillard and Fuller used an array of accelerometers and digital signal processing to achieve the desired wave-number filtering.[7] This is accomplished by passing the accelerometer information through an array of finite impulse response filters that process the data to provide information on specific wave-number components. The wave-number filtering is achieved through software, as opposed to distributed sensors.

This paper presents results of a numerical investigation using an array of shaped PVDF sensors to act as low-pass

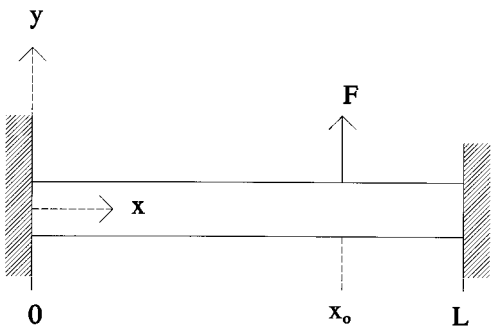

FIG. 1. Schematic of beam geometry for the system.

filters of the spatial strain transform. An analytical model of a clamped-clamped Bernoulli–Euler beam is presented to obtain the beam's strain response, which is then used to obtain the response of point and distributed sensors. The choice of the distributed sensor shape is also investigated. Finally, the radiated power estimates using point and distributed sensors are compared to those predicted by theory.

I. ACOUSTIC RADIATION FROM STRUCTURES

The one-sided far-field acoustic power per unit width radiated from a beam undergoing sinusoidal vibration can be expressed as

$$\Pi = \frac{\omega \rho_f}{4\pi} \int_{-k_f}^{k_f} \frac{|V(k_x)|^2}{\sqrt{k_f^2 - k_x^2}}\, dk_x, \tag{1}$$

where ω is the angular frequency, ρ_f is the fluid density, $V(k_x)$ is the spatial Fourier transform of the beam velocity, k_x is the beam wave number, and k_f is the total fluid wave number.[8] Equation (1) shows that only the wave number components with magnitude less than or equal to k_f, which are referred to as supersonic wave numbers, contribute to the far-field sound radiation. Therefore, if a suitable velocity wave-number spectrum is obtained, an estimate of the radiated power from the structure can be made using Eq. (1). Since the strain in the beam is related to the displacement, and hence the velocity, the strain wave-number transform can also be used to estimate the radiated power of the beam.

A. System model

The system studied is a Bernoulli–Euler damped beam of length L with clamped ends (see Fig. 1). The equation of motion for this system can be expressed as

$$E^* I \frac{\partial^4 \xi(x,t)}{\partial x^4} + m \frac{\partial^2 \xi(x,t)}{\partial t^2} = F_0 \delta(x - x_0) e^{j\omega t},$$
$$E^* = E(1 + j\eta), \quad I = bh^3/12, \tag{2}$$

where ξ is the displacement in the y direction, E is the Young's modulus, I is the second moment of the cross-sectional area for a rectangular cross section, m is the mass per unit length of the beam, F_0 is the magnitude of the forcing function, $\delta(x)$ is the Dirac delta function, η is the damping loss factor, b is the width of the beam, and h is the beam thickness. The specific beam values used in the analytical model are presented in Table I.

TABLE I. Beam parameters used in the theoretical model.

Parameter	Symbol	Value
Length	L	0.914 m
Width	w	0.0508 m
Height	h	0.006 35 m
Young's modulus	E	71 GPa
Mass density	ρ	2700 kg/m^3
Damping loss factor	η	0.05

B. Natural frequencies

The transcendental equation for the system, obtained by setting the forcing function to zero in Eq. (2) and applying the appropriate boundary conditions, is

$$\cosh(k_b L)\cos(k_b L) = 1,$$
$$k_b = \left(\frac{\rho\omega^2}{E^*\kappa^2}\right)^{1/4}, \quad \kappa = \frac{h}{\sqrt{12}}, \tag{3}$$

where k_b is the beam bending wave number ρ is the mass density of the beam, and κ is the radius of gyration for a rectangular section.[9] To obtain the undamped natural frequencies, the damping loss factor was set to zero in the transcendental equation. The first five roots for $k_b L$ and their corresponding frequencies are shown in Table II.

C. Forced solution

The equation of motion can also be solved to obtain an expression for the beam displacement response. Polyvinylidene fluoride (PVDF) generates a voltage signal that is proportional to the strain. Therefore, an analytical expression for strain is desired. The strain, ϵ, can be obtained from the displacement using the relationship

$$\epsilon(x,t) = -y \frac{\partial^2 \xi(x,t)}{\partial x^2} = \begin{cases} \epsilon_1(x,t), & x = [0, x_1], \\ \epsilon_2(x,t), & x = [x_1, L], \end{cases}$$
$$\epsilon_1(x,t) = -y k_b^2 \{A_1[\cosh(k_b x) + \cos(k_b x)] + B_1[\sinh(k_b x) + \sin(k_b x)]\} e^{j\omega t}, \tag{4}$$
$$\epsilon_2(x,t) = -y k_b^2 \{A_2 \cosh[k_b(x - x_1)] + B_2 \sinh[k_b(x - x_1)] - C_2 \cos[k_b(x - x_1)] - D_2 \sin[k_b(x - x_1)]\} e^{j\omega t}.$$

Here, y is the distance from the neutral axis; the subscripts 1

TABLE II. Roots and frequencies of beam characteristic equation.

Mode	$k_b L$	Frequency (Hz)
1	4.73	40.07
2	7.85	110.45
3	11.00	216.52
4	14.14	357.92
5	17.28	534.67

and 2 refer to the beam sections before and after the excitation point, respectively; $x=0$ refers to the left-hand side of each section; and $x_1=x_0$ and $x_2=L-x_0$ refer to the right-hand side of sections one and two, respectively. The subscripted letters in Eqs. (4) are constants defined as

$$A_1=\frac{F}{E^*Ik_b^3V_8},\quad B_1=V_3A_1,\quad A_2=V_4A_1,\quad B_2=V_7A_1,\quad C_2=V_5A_1,\quad D_2=V_6A_1, \tag{5}$$

and the V_i terms are constants given by

$$V_1=\frac{(\mathrm{sh}_1+\mathrm{si}_1)(\mathrm{sh}_2\,\mathrm{co}_2-\mathrm{ch}_2\,\mathrm{si}_2)-(\mathrm{ch}_1-\mathrm{co}_1)(\mathrm{sh}_2\,\mathrm{si}_2-\mathrm{ch}_2\,\mathrm{co}_2-1)}{2(1-\mathrm{ch}_2\,\mathrm{co}_2)},$$

$$V_2=\frac{(\mathrm{ch}_1-\mathrm{co}_1)(\mathrm{sh}_2\,\mathrm{co}_2-\mathrm{ch}_2\,\mathrm{si}_2)-(\mathrm{sh}_1-\mathrm{si}_1)(\mathrm{sh}_2\,\mathrm{si}_2-\mathrm{ch}_2\,\mathrm{co}_2-1)}{2(1-\mathrm{ch}_2\,\mathrm{co}_2)},$$

$$V_3=\frac{V_1-\mathrm{ch}_1}{\mathrm{sh}_1-V_2},\quad V_4=V_1+V_2V_3,\quad V_5=\mathrm{ch}_1-\mathrm{co}_1+(\mathrm{sh}_1-\mathrm{si}_1)V_3-V_4, \tag{6}$$

$$V_6=\frac{V_4+(\mathrm{sh}_2\,\mathrm{si}_2-\mathrm{ch}_2\,\mathrm{co}_2)V_5}{\mathrm{sh}_2\,\mathrm{co}_2-\mathrm{ch}_2\,\mathrm{si}_2},\quad V_7=-\frac{V_4\,\mathrm{ch}_2+V_5\,\mathrm{co}_2+V_6\,\mathrm{si}_2}{\mathrm{sh}_2},\quad V_8=-\mathrm{sh}_1+\mathrm{si}_1-(\mathrm{ch}_1+\mathrm{co}_1)V_3-V_6+V_7.$$

For compactness, Eqs. (6) and subsequent equations use the following notation to express frequently occurring trigonometric and hyperbolic constants:

$$\mathrm{si}_i=\sin(k_bx_i),\quad \mathrm{co}_i=\cos(k_bx_i),\quad \mathrm{sh}_i=\sinh(k_bx_i),\quad \mathrm{ch}_i=\cosh(k_bx_i), \tag{7}$$

where the index, i, can take the value 1 or 2. The spatial Fourier transform of the strain, $E(k_x,t)$, is given by

$$\begin{aligned}E(k_x,t)=\int_0^L\epsilon(x,t)e^{-jk_xx}\,dx=-yk_b^2\Bigg\{&\frac{A_1}{k_b^2+k_x^2}[(k_b\,\mathrm{sh}_1+jk_x\,\mathrm{ch}_1)e^{-jk_xx_1}-jk_x]-\frac{A_1}{k_b^2-k_x^2}[(-k_b\,\mathrm{si}_1+jk_x\,\mathrm{co}_1)e^{-jk_xx_1}-jk_x]\\&+\frac{B_1}{k_b^2+k_x^2}[(k_b\,\mathrm{ch}_1+jk_x\,\mathrm{sh}_1)e^{-jk_xx_1}-k_b]-\frac{B_1}{k_b^2-k_x^2}[(k_b\,\mathrm{co}_1+jk_x\,\mathrm{si}_1)e^{-jk_xx_1}-k_b]\\&+\frac{A_2}{k_b^2+k_x^2}[(k_b\,\mathrm{sh}_2+jk_x\,\mathrm{ch}_2)e^{-jk_xL}-jk_xe^{-jk_xx_1}]+\frac{B_2}{k_b^2+k_x^2}[(k_b\,\mathrm{ch}_2+jk_x\,\mathrm{sh}_2)e^{-jk_xL}\\&-k_be^{-jk_xx_1}]-\frac{C_2}{k_b^2-k_x^2}[(k_b\,\mathrm{si}_2-jk_x\,\mathrm{co}_2)e^{-jk_xL}+jk_xe^{-jk_xx_1}]\\&-\frac{D_2}{k_b^2-k_x^2}[(k_b\,\mathrm{co}_2+jk_x\,\mathrm{si}_2)e^{-jk_xL}+k_be^{-jk_xx_1}]\Bigg\}e^{j\omega t}.\end{aligned} \tag{8}$$

A typical strain response and strain transform spectrum is shown in Fig. 2 for a unit force located at $x_0=0.64$ m.

II. POWER IN TERMS OF THE STRAIN TRANSFORM

Given the strain transform, it is desirable to obtain an expression for radiated power in terms of this quantity. Making use of the relationship between the Fourier transform of a function, $F(k_x)$, and the Fourier transform of the nth derivative of this function, $f^{(n)}(x)$,[10] namely

$$\mathscr{F}\{f^{(n)}(x)\}=(jk_x)^nF(k_x), \tag{9}$$

the displacement and strain transforms are related by the equation

$$E(k_x)=yk_x^2D(k_x). \tag{10}$$

Using Eq. (10) and assuming $e^{j\omega t}$ time dependence, the power can be written in terms of the strain transform. This equation is

$$\Pi=\frac{\omega^3\rho_f}{4\pi y^2}\int_{-k_f}^{k_f}\frac{|E(k_x)|^2}{k_x^4\sqrt{k_f^2-k_x^2}}\,dk_x. \tag{11}$$

III. POINT SENSORS VERSUS DISTRIBUTED SENSORS

Individual strain sensors must be used to obtain an estimate of the beam wave-number spectrum. If point sensors are used, a sufficiently large number of sensors must be used to resolve the highest wave-number components of the wave-number spectrum. This number is based on the Nyquist criterion and if it is not met, then aliasing problems occur.

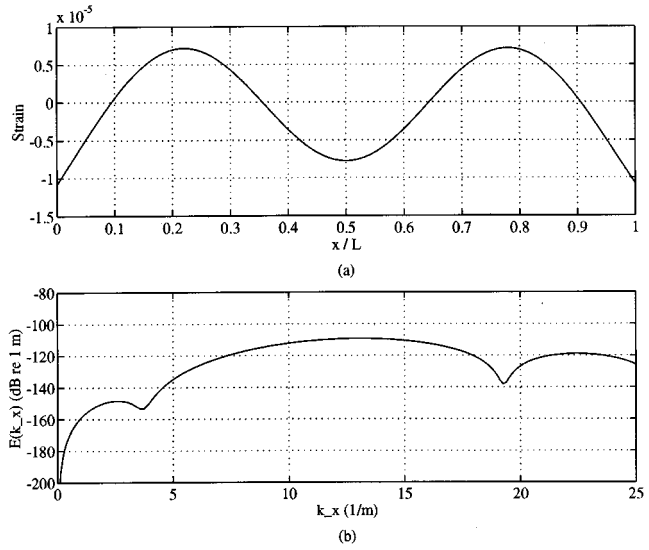

FIG. 2. Theoretical (a) strain and (b) Fourier transform of strain for resonance 3.

The Nyquist criterion specifies that a minimum of two sensors per wavelength must be used for the shortest wavelength that exists.

The number of sensors required to obtain a wave-number spectrum estimate without aliasing problems can be reduced by the use of distributed sensors. Distributed sensors can be fabricated to reduce the sensitivity of the sensors to higher wave-number components. In this way, the aliasing is reduced and the number of sensors used can potentially be reduced.

A distributed strain sensor placed on the beam will output an electric signal proportional to the integrated strain over the area of the sensor. In equation form this proportion can be written as

$$\epsilon_d(x_s,t)=\int_{x_s-a}^{x_s+b}\epsilon(x,t)s(x)dx, \tag{12}$$

where ϵ_d is the distributed strain result; x_s is the center position of the sensor, x_s-a and x_s+b correspond to the minimum and maximum locations of the patch, respectively, and $s(x)$ is an arbitrary shape function. The form of the shape function used in this research is discussed in the next section.

IV. THE SHAPE FUNCTION

A distributed strain sensor effectively integrates the strain over the sensor area and a shape function can be introduced to vary the width of the sensor. This shape function can be chosen to provide spatial filtering. For this paper the shape function was chosen to provide low-pass filtering in the wave-number domain and is defined as

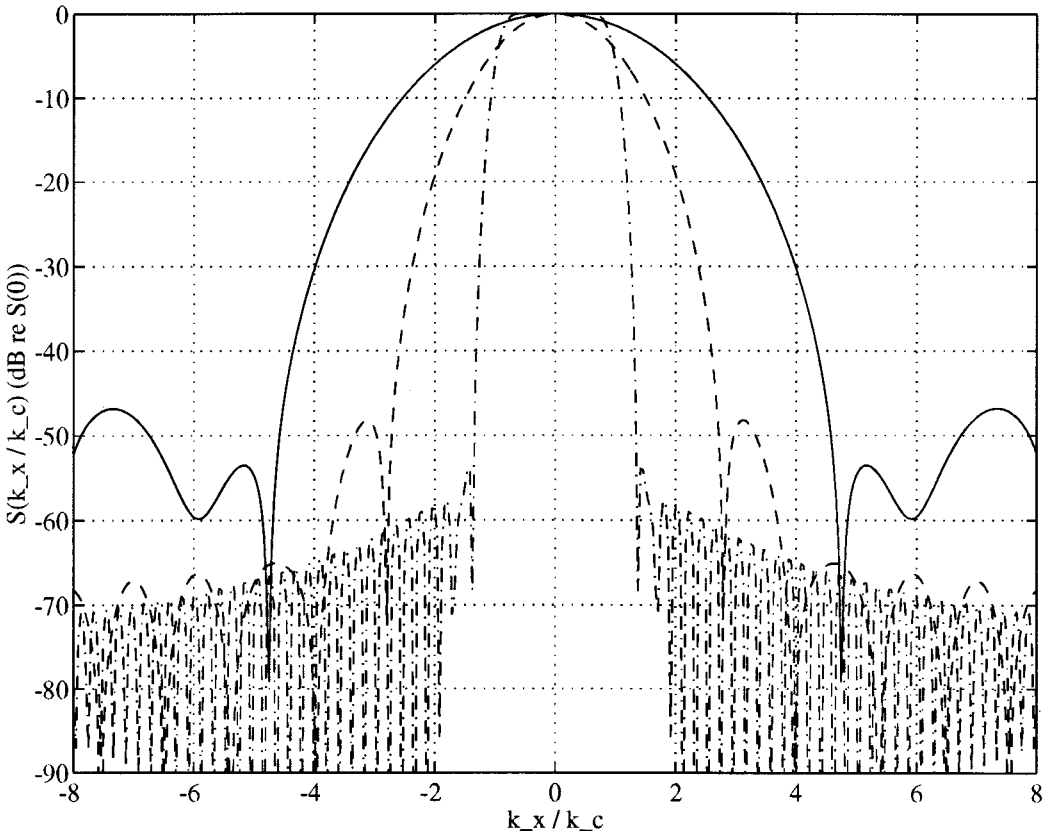

FIG. 3. Wave-number response of shape function. ($k_c l_p$) values shown are ——— 3, –– 6, and –·– 30.

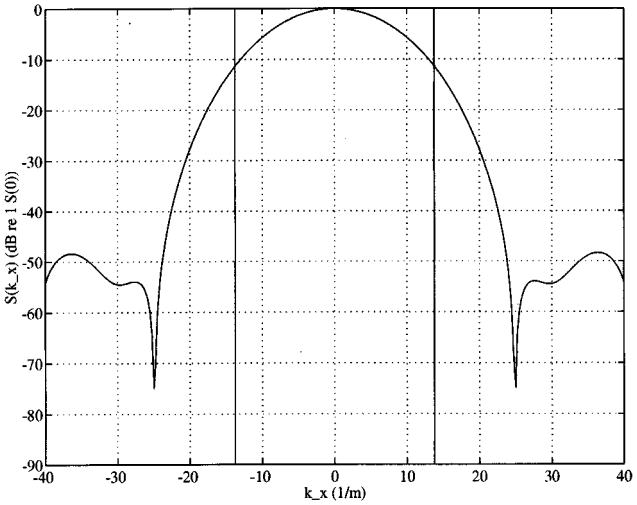

FIG. 4. Wave-number response of shape function for $l_p = 0.6$ m and $k_c = 6\ \mathrm{m}^{-1}$. The solid vertical lines indicate the Nyquist wave numbers.

$$s(x) = h(x - x_s)\,\mathrm{sinc}[k_c(x - x_s)],$$

$$h(x) = \begin{cases} 0.54 + 0.46\cos\left(2\pi\dfrac{x}{l_p}\right), & -a \leqslant x \leqslant b, \\ 0, \quad x < -a, \ x > b, \end{cases} \tag{13}$$

$$\mathrm{sinc}(x) = \frac{\sin(x)}{x},$$

where $h(x)$ defines a Hamming window,[11] k_c is the positive cutoff wave number, and l_p is the full sensor length. Note that l_p is the Hamming window length determined to provide the desired wave-number filter characteristics and is not necessarily equal to $a+b$. For example, if $s(x, x<0)$ is not part of the structure and $s(x, x \geqslant 0)$ is part of the structure, then $a=0$ and $b=l_p/2$. The corresponding Fourier transform of the shape function is

$$S(k_x) = \int_{-a}^{b} s(x) e^{-jk_x x}\, dx. \tag{14}$$

The sinc function provides the low-pass filter characteristics for the wave-number spectrum. A nontruncated sinc function would provide perfect low-pass wave-number filtering of the signal, while a finite function length causes the resulting signal to be nonzero for the domain $|k_x| > k_c$. The Hamming window was chosen to provide a smooth roll-off of the signal to minimize leakage when the discrete Fourier transform is used.

A closed-form solution for the integral of Eq. (14) is not possible. However, by making use of the convolution properties of the Fourier transform, the perfect low-pass property of the sinc function and the finite window length $S(k_x)$ can be written in terms of the Fourier transform of the Hamming window. The resulting expression is given by

$$S(k_x) = \frac{e^{-jk_c x_s k_x}}{k_c} \int_{k_x - k_c}^{k_x + k_c} e^{j(k_c - 1)x_s \beta} H(\beta)\, d\beta, \tag{15}$$

where $H(k_x)$ is the Fourier transform of the Hamming window. For the special case of $x_s = 0$, Eq. (15) reduces to

$$S(k_x) = \frac{1}{k_c} \int_{k_x - k_c}^{k_x + k_c} H(\beta)\, d\beta. \tag{16}$$

Figure 3 plots the function $S(k_x)$ in Eq. (16) for various values of $k_c l_p$ and $a = b = l_p/2$.

TABLE III. Location of point and patch sensors on the beam.

Patch number	$x_s - a$ (m)	x_s (m)	$x_s + b$ (m)
1	0	−0.114	0.186
2	0	0.114	0.414
3	0.043	0.343	0.643
4	0.271	0.571	0.871
5	0.500	0.800	0.914
6	0.728	1.028	0.914

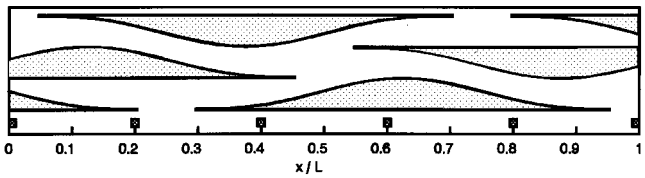

FIG. 5. Schematic showing patch and point sensor locations on the beam. Squares indicate point sensors.

V. NUMERICAL MODEL AND SIMULATIONS

The desire is to design an array of distributed sensors that can be used to estimate a beam's radiated power over a given frequency range. Since the array is intended to be used over a range of frequencies, the tuning of the system to a specific frequency or set of frequencies is not an acceptable solution. The three design parameters considered are the number of sensors, the full patch length, and the cutoff wave number.

A. Description of model and parameters

The beam system is identical to that outlined in Sec. I. The amplitude of the forcing function is set to unity and the forcing location is 0.64 m (0.7 L) for all runs. The frequency

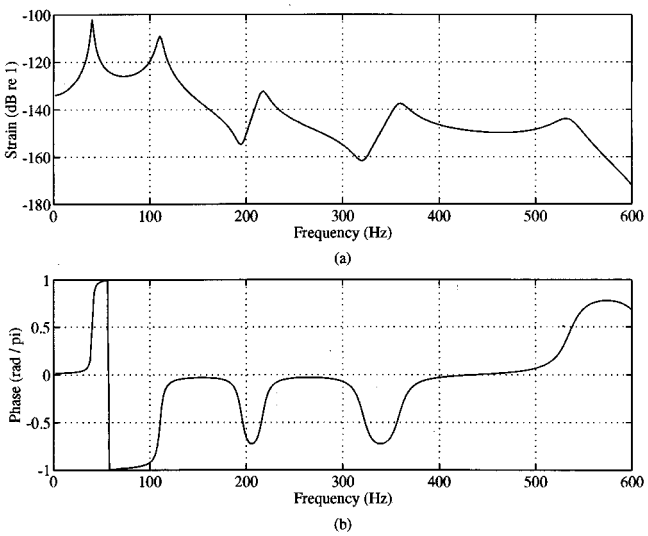

FIG. 6. Numerical frequency response for patch 3. (a) Magnitude and (b) phase.

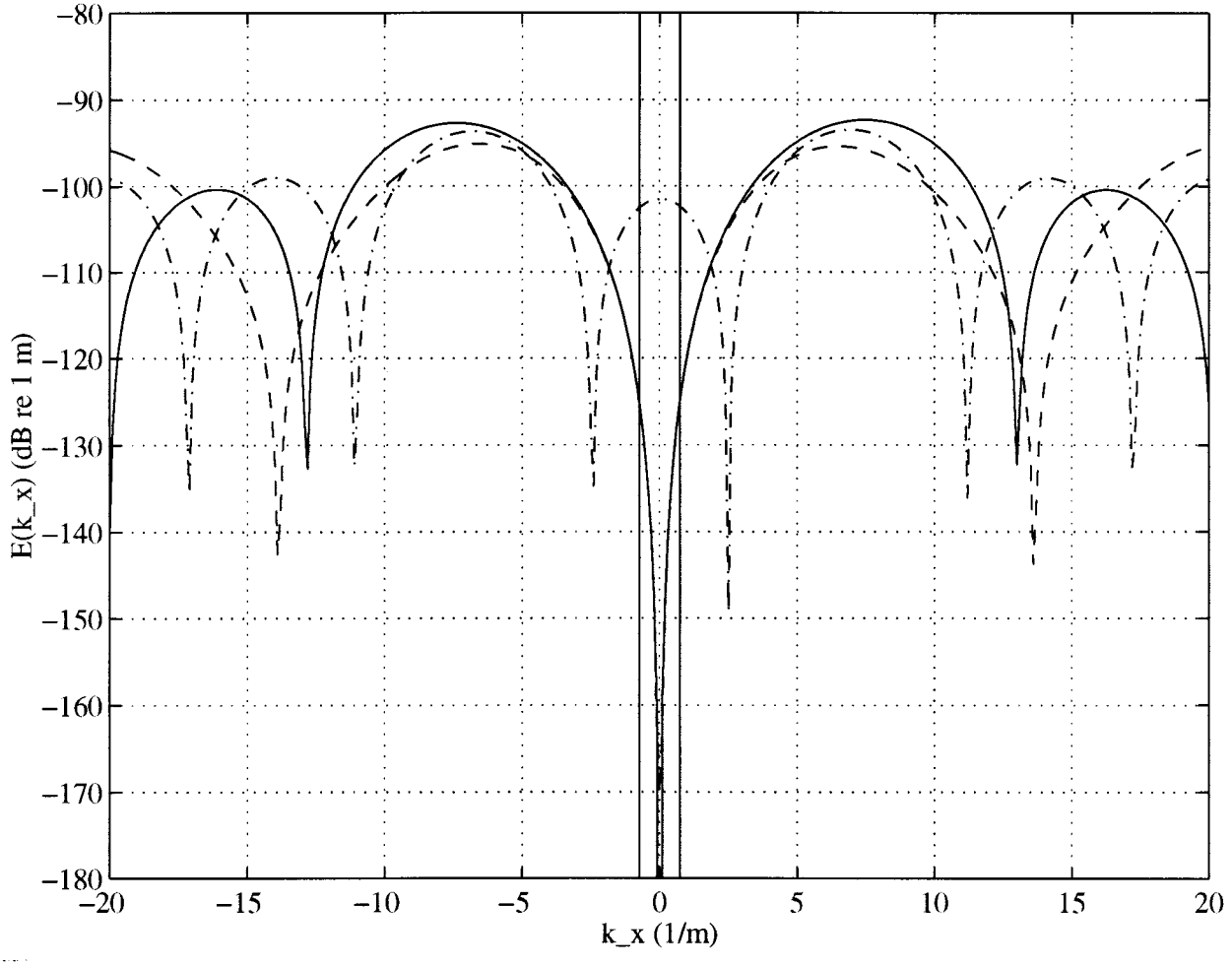

FIG. 7. Fourier transform of strain response for resonance 1 (40.07 Hz). Legend: ——— theoretical response, –– patch response, –·– point response, and | acoustic wave number.

of the forcing function changes for the various tests carried out. To determine the number of sensors required, one must first calculate the center to center sensor spacing Δx, which is dependent upon the highest fluid wave number to be included in the analysis. The application of interest in this paper is active control of radiation from structures, and is thus concerned primarily with the low-frequency behavior of the beam. Therefore, analysis will be limited to radiation into air for frequencies only up to the fifth beam resonance frequency.

Using a fluid wave speed of 343 m/s and a value of 535 Hz for the fifth resonance frequency, the highest wave number of interest is 9.8 m^{-1}. The maximum sensor spacing allowed to sufficiently sample up to this wave number, as set forth by the Nyquist criterion, is 0.32 m. Using this sensor spacing and requiring that the first and last sensors whose center positions, x_s, are located on the beam be placed $\Delta x/2$ m from the beam ends, the minimum number of sensors required is three. A margin of safety is added by specifying that there be at least four sensors with center positions on the beam. The resulting sensor spacing is 0.23 m, which can resolve wave numbers up to 13.75 m^{-1}.

The next parameters to be calculated are the patch length and cutoff wave number, which define the shape function. These two parameters are chosen to attenuate the wave-number components above the highest wave number resolvable as calculated above. Ideally, the sensors would provide very large attenuation above the design cutoff wave number, such as that provided by the $(k_c l_p)=30$ curve in Fig. 3. However, if a cutoff wave number of 9.8 m^{-1} is chosen, the corresponding patch length of 3.06 m becomes excessively large for the beam. Alternatively, if a more reasonable patch length of 0.5 m is chosen, then the corresponding cutoff wave number of 60 m^{-1} becomes excessively large for the sensor spacing chosen.

A compromise between the patch length and cutoff wave number must be made. A patch length of 0.6 m and a cutoff wave number of 6 m^{-1} provides a reasonable compromise. This combination of parameters provides attenuation of approximately 6 dB at 9.8 m^{-1}, approximately 11 dB at 13.75 m^{-1}, and 20 dB or more for wave numbers above 18 m^{-1} (see Fig. 4). Although these attenuation levels are not as high as one might desire, the length and cutoff wave-number values chosen provide sufficient attenuation of higher wave numbers to obtain reasonable estimates of the spectrum over the frequency and wave-number range of interest.

To estimate the radiated power, the frequency domain

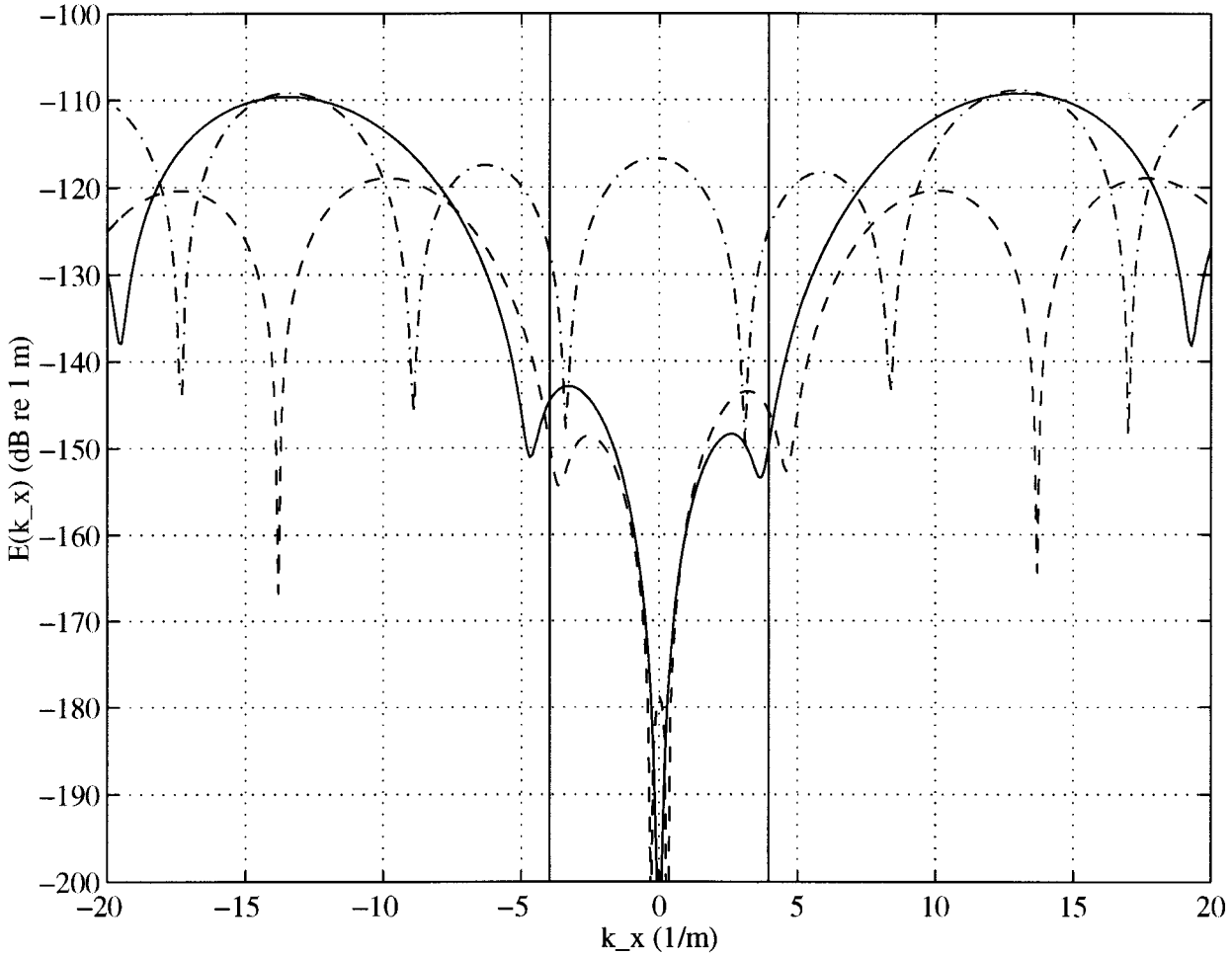

FIG. 8. Fourier transform of strain response for resonance 3 (216.52 Hz). Legend: ——— theoretical response, –– patch response, –·– point response, and | acoustic wave number.

response of each patch is obtained from the time-domain signal using a temporal Fourier transform. A spatial discrete Fourier transform (DFT) of the array of frequency domain signals then provides an estimate of the wave-number spectrum. Given the excitation frequency, the fluid wave number can be determined. This fluid wave number and the wave-number spectrum can then be used to estimate the radiated power by implementing Eq. (11).

The full patch length of 0.6 m means that there are six full or partial patches on the beam. Table III provides the center and end-point locations for each patch and Fig. 5 shows a schematic of the patch locations on the beam.

For comparison purposes, point strain sensors on the beam are also modeled. Six equally spaced point sensors were placed along the length of the beam. The locations of these sensors on the beam are 0, 0.183, 0.366, 0.548, 0.731, and 0.914 m (see Fig. 5). Note that no consideration was given to the optimal placement of the point sensors.

B. Numerical results

Two types of numerical tests were carried out. The first is a frequency response for each patch. This was accomplished by sweeping the driving frequency of the force over the desired frequency range and recording the response level of each patch. The frequency response of patch 3 is shown in Fig. 6.

The second type of test is a spatial DFT of the six patches at a given frequency, which corresponds to the strain wave-number transform. First the model was driven at 40.07 Hz, which corresponds to the first beam resonance frequency, and the patch levels recorded. A DFT of the data was then taken to obtain a strain transform spectrum. This procedure was repeated for the frequencies 110.45, 216.52, 357.92, and 534.67 Hz, which correspond to the next four resonance frequencies of the beam. In addition to the patch strain transforms, the theoretical and point strain transforms were also calculated for these frequencies. Sample plots of these results are shown in Figs. 7–9. Next, the excitation frequency was set to 75, 160, 300, and 450 Hz, which are frequencies approximately midway between the resonance frequencies, and again a DFT of the strain results was calculated. Samples of these results are shown in Figs. 10 and 11.

Two items must be noted concerning these plots. First, to offset the attenuation of the strain field due to the shape function, the shape function was normalized so that the integral of the shape function for a full patch was unity,[12] i.e.,

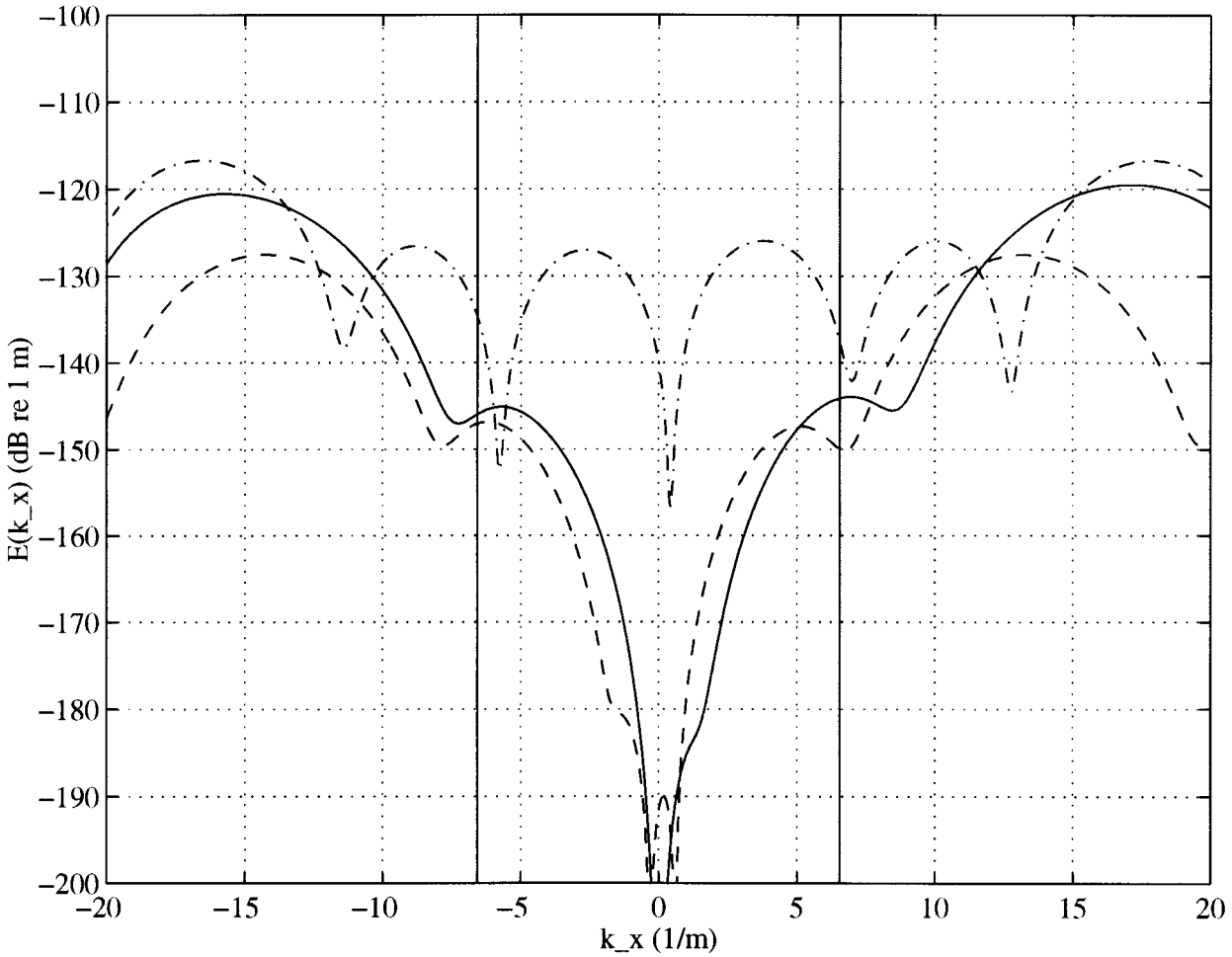

FIG. 9. Fourier transform of strain response for resonance 4 (357.92 Hz). Legend: ——— theoretical response, −− patch response, −·− point response, and | acoustic wave number.

$$\int_{-0.3}^{0.3} s(x)dx = 1. \tag{17}$$

The application of this normalization introduces a shift of 10.5 dB to the filtered strain transforms. Second, to account for aliasing associated with the point sensors, the point strain transforms were shifted by −5.4 dB. This number represents the average overestimation of the point sensors at the first four resonance and first two off-resonance frequencies when compared to the maximum level of the theoretical strain transforms. The use of this correction for the point spectra assumes that the maximum level of the point spectrum should match the maximum level of the theoretical spectrum if the peak of the theoretical spectrum lies below the point Nyquist wave number.

The final computations involve calculating the integral of $|E(k_x)|^2$ over the range of supersonic wave numbers and estimating the radiated power from the beam using the strain transform results. Specific strain integrals were evaluated at the first five resonance frequencies and four frequencies between the resonance frequencies. Power estimates were obtained by performing a frequency sweep and implementing Eq. (11). The integral calculations use Simpson's 1/3 rule[13] to approximate the strain transform integral and the integral in Eq. (11). To circumvent problems associated with the poles at $-k_f$, 0, and k_f of the radiated power equation, the range of integration used was $-0.95k_f \leqslant k_x \leqslant -0.05k_f$ and $0.05k_f \leqslant k_x \leqslant 0.95k_f$. Each wave-number range was then divided into 50 equally spaced intervals and the theoretical, patch, and point transforms calculated. Shift factors were applied to the point and distributed strain transforms, as explained in the preceding paragraph. The results of the point and patch strain integral are presented in Table IV. The power predictions are presented in Fig. 12.

C. Discussion

The frequency response for patch 3 (Fig. 6) clearly shows the expected first five resonances of the beam.

The strain transforms (Figs. 7–11) show that the patch results follow the theoretical values reasonably well for structural wave numbers below the fluid wave number, while the point results show significant differences from the theoretical results, not only in level, but also in form. Examining the predicted response at the first resonance frequency (Fig. 7) shows a number of key elements. The theoretical values go to zero at low wave numbers. This is an expected result, given the relationship between the strain and displacement

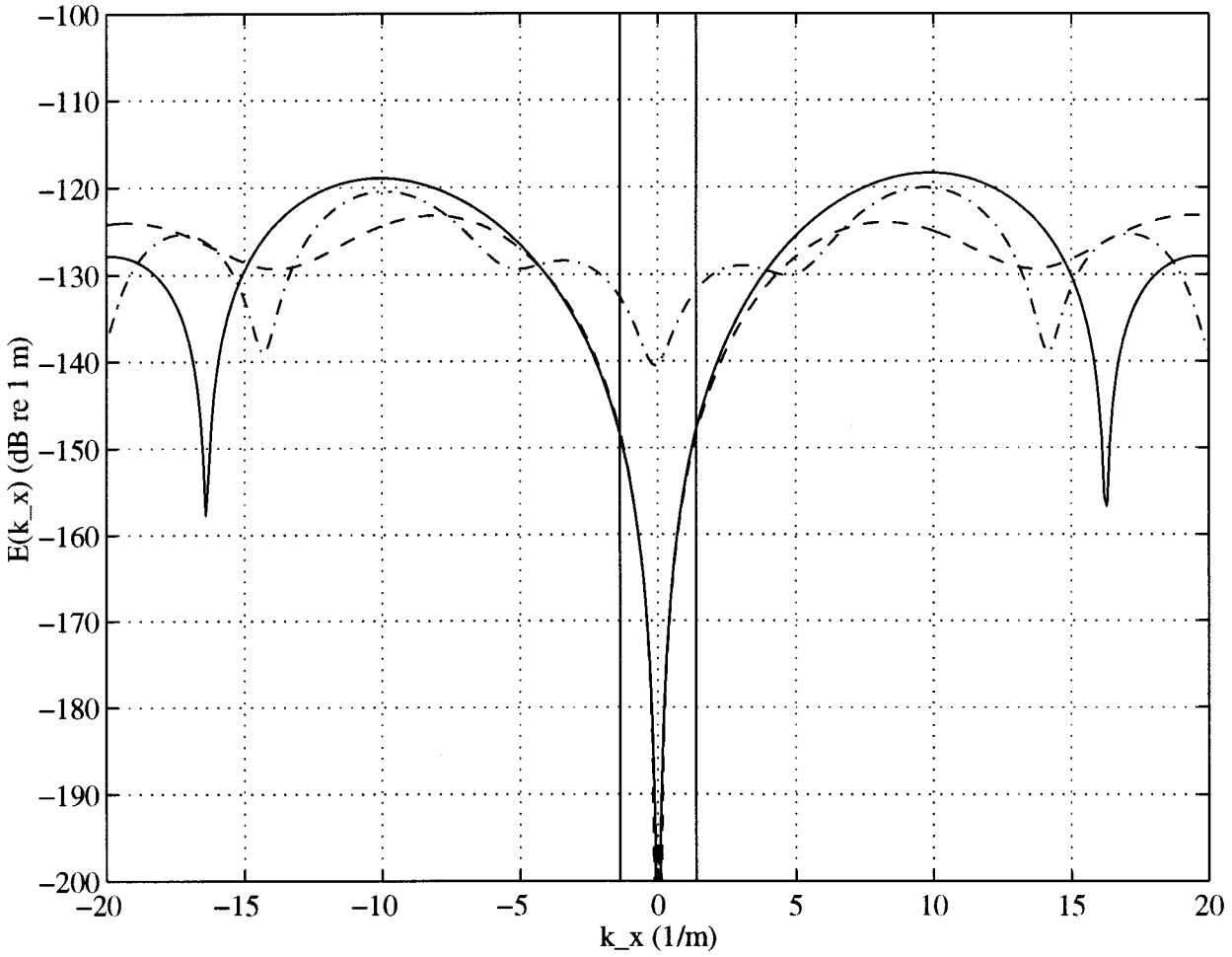

FIG. 10. Fourier transform of strain response for 75 Hz. Legend: ——— theoretical response, –– patch response, –·– point response, and | acoustic wave number.

spatial transforms [see Eq. (10)] and is expected for all frequencies. The patch results show excellent agreement with the theoretical results. The patch result tends towards zero at low wave numbers with a level of approximately -170 dB at $k_x=0$. Conversely, the point results differ sharply from the theoretical values. The point result has a local maximum level near zero wave number and does not follow the shape of the analytical solution below the fluid wave number. This high level at low wave number is due to aliasing problems associated with the point sensors.

Given the sensor spacing and using the Nyquist criterion, the highest wave numbers that the point and patch arrays can resolve are 17.19 and 13.75 m^{-1}, respectively. As can be seen from the theoretical curve, the strain transform levels are high above these k_{max} values. Unlike the patches, which provide wave-number filtering to reduce the level of the high wave-number components, the point sensors provide no filtering and all of the wave-number components above k_{max} are aliased back to the lower spectral lines. Another aspect that is apparent in Fig. 7 is the wrapping characteristic associated with the DFT. Both the point and patch results show a symmetry about their respective k_{max} values.

Looking at the results of the third resonance (Fig. 8), one sees that the patch array has a similar shape to the theoretical curve. However, the locations and levels of their maxima do not correspond. The patch response overestimates the theoretical value by approximately 6 dB for positive wave numbers and underestimates the theoretical level by a similar amount for negative wave numbers. A deviation at low wave number is noticeable on the patch curve. However, this deviation occurs in the vicinity of -180 dB and does not have a significant effect on the overall shape of the curve. The point curve does not follow the shape of the theoretical curve and again has a high response at low wave numbers.

The response at the fourth resonance (Fig. 9) also shows a marked difference between the theory and patch levels. The levels of the patch response are higher than the theoretical values from a wave number of approximately 0.6–5 m^{-1} and lower than the theoretical values from 5 m^{-1} up to the maximum wave number of interest, which is the fluid wave number at 6.56 m^{-1}. The patch level falls below the theoretical level for most of the negative wave-number range of interest. The point levels are again significantly different from the theoretical values, with the maximums occurring well before the theoretical values.

The off-resonance response plots show similar results to the resonance plots. That is, the patch results follow the the-

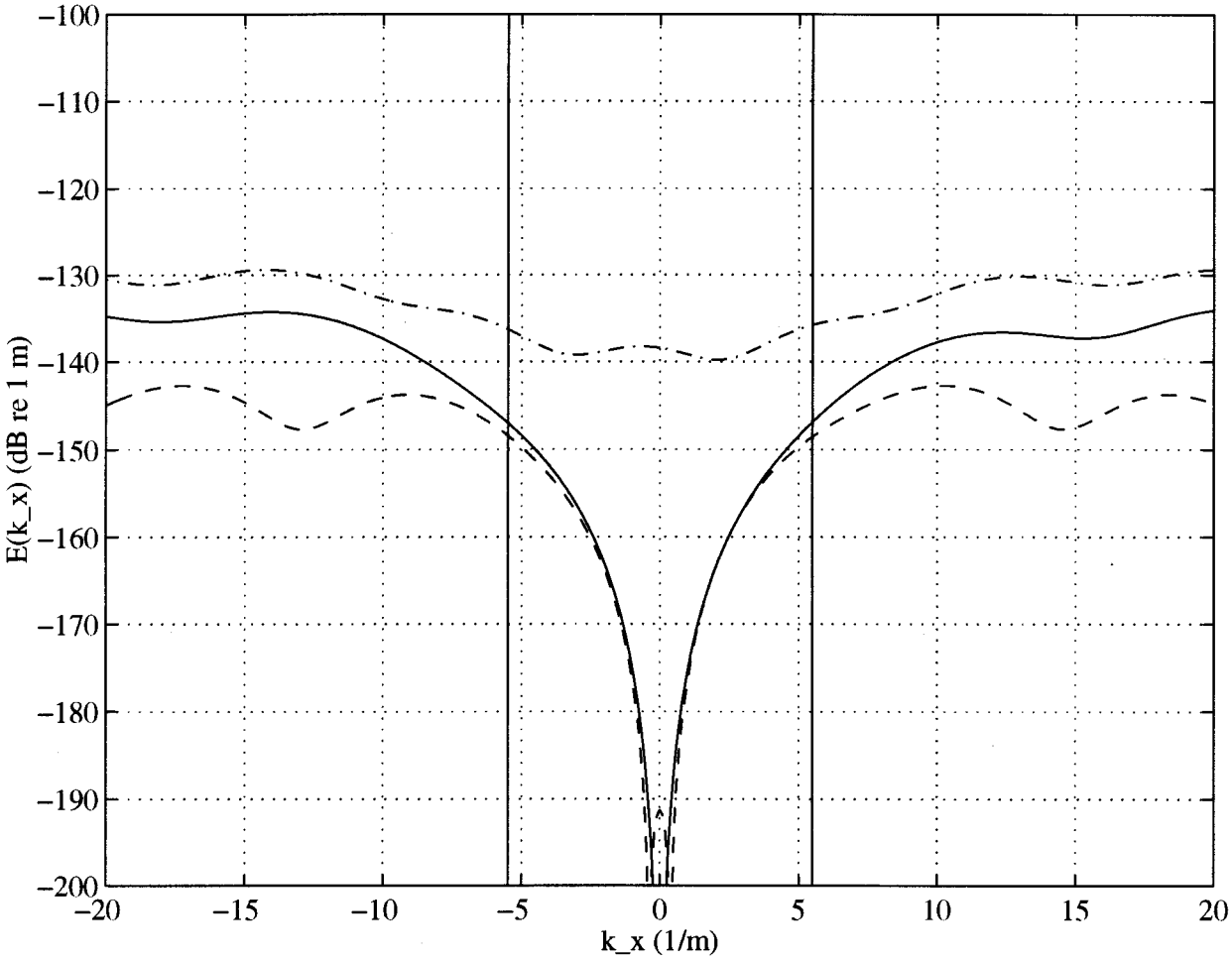

FIG. 11. Fourier transform of strain response for 300 Hz. Legend: ——— theoretical response, –– patch response, –·– point response, and | acoustic wave number.

oretical curve below the fluid wave number while the point response is affected by aliasing. The aliasing problem for the point array seems to be apparent at each driving frequency and could be due to the mixture of multiple modes of the beam. As before, the low wave-number deviations in the patch response become more pronounced at higher frequencies, but are still well below the maximum levels.

The values for the integrals of the squared magnitude of the strain transform in Table IV show that the patch results range from −1.6 to 3.0 dB when compared to the theoretical results. These deviations from the theoretical results, which are the integral estimates for resonances four and five, are not surprising considering the differences in the strain transforms predicted by theory and the patch array. Predictions for the other frequencies studied are all within 1 dB of the theoretical result. Unlike the patch results, the integral using the point sensors overestimated the theoretical values by 15.8–30.9 dB. These high overestimation predictions are caused by aliasing problems associated with the point array.

TABLE IV. Integral of magnitude squared strain transform for patch and point arrays.

	$\int\|E(k_x)\|^2\, dk_x$ (dB *re*: theory)	
Frequency (Hz)	Patch sensors	Point sensors
40.07	−0.1	30.9
110.45	−0.4	26.5
216.52	−0.4	27.6
357.92	−1.6	20.9
534.67	3.0	19.5
75	−0.1	20.2
160	−0.4	20.6
300	−1.0	15.8
450	0.7	19.5

Since the ultimate goal of this research is to determine if shaped sensors can provide a means for obtaining an acceptable estimation of the radiated power, the power results presented in Fig. 12 provide an excellent criterion for assessing the performance of the point and patch sensors. As with the results for the integrals of the squared magnitude, the power calculations show the power calculations using the patch sensors are significantly better than the power results using the point sensors, when compared to the theoretical values. Both the point and patch results show a marked increase in predicted radiated power at low frequencies. However, if only the frequency range between 20 and 600 Hz is consid-

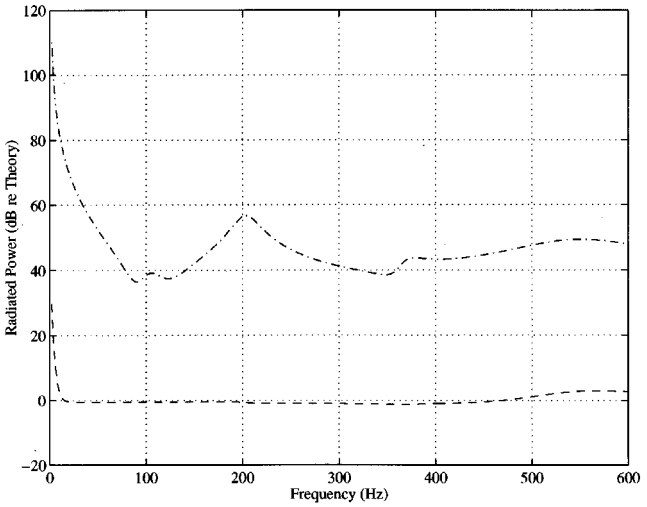

FIG. 12. Estimated power of patch and point arrays. Legend: –– patch response and –·– point response.

ered, the spread for the patch sensor estimates is −1 to 3 dB, while the point sensor estimates have a spread of 36–68 dB.

VI. CONCLUSIONS

This paper presents a technique to obtain the far-field radiated power from a one-dimensional structure using an array of shaped polyvinylidene fluoride sensors. The distributed sensors are shaped to act as low-pass wave-number filters, since the radiated power depends only on the structural wave-number components whose magnitudes are less than or equal to the fluid wave number.

The results show that the shaped sensors provide a better approximation to the theoretical strain transform than do the point sensors. This is verified by the form of the functions, presented by plotting the individual strain transforms, and by integrating the squared magnitude of the strain transforms and comparing the results to the theoretical values. Overall, these results indicate good agreement with the analytical predictions. The errors for the integral of the squared magnitude of the strain transforms are all 3 dB or less when using the shaped sensors, compared to at least 15.8 dB when using the point sensors.

Power estimates using the strain transform results show that patch estimations are again considerably better than the point estimations when compared to the theoretical predictions. The power results indicate that the use of shaped sensors, as described in this paper, can provide a better estimate of a structure's radiated power than the use of discrete point sensors. The estimated powers using the shaped sensors are all within 3 dB of the actual power for most of the frequency range, while those using discrete point sensors overestimate the level by at least 36 dB for the same frequency range. These results indicate the ability for shaped sensors to provide significantly improved power estimates for applications that estimate radiated power from structural measurements.

ACKNOWLEDGMENTS

This work was supported by the Applied Research Laboratory at The Pennsylvania State University and the Acoustical Society of America.

[1] S. E. Burke, ''Distributed transducer shading: Application to structural control, hydrodynamics, and sonar sensing,'' Proc. SPIE **1917**, 660–673 (1993).
[2] S. E. Burke and J. E. Hubbard, Jr., ''Distributed transducer vibration control of thin plates,'' J. Acoust. Soc. Am. **90**, 937–944 (1991).
[3] C.-K. Lee and F. C. Moon, ''Modal sensors/actuators,'' J. Appl. Mech. **57**, 434–441 (1990).
[4] S. A. Collins, D. W. Miller, and A. H. von Flotow, ''Piezopolymer Spatial Filters for Active Structural Control,'' in *Proceedings of the Conference on Recent Advances in Active Control of Sound and Vibration*, edited by C. A. Rogers and C. R. Fuller (Technomic, Lancaster, PA, 1991), pp. 219–234.
[5] D. W. Miller, S. A. Collins, and S. P. Peltzman, ''Development of Spatially Convolving Sensors for Structural Control Applications,'' Collection of Technical Papers—AIAA/ASME/ASCE/AHS Structures, Structural Dynamics & Materials Conference, Part 4 (American Institute of Aeronautics and Astronautics, Washington, DC, 1990), pp. 2283–2297.
[6] M. S. Anderson and E. F. Crawley, ''Discrete Shaped Strain Sensors for Intelligent Structures,'' Proceedings of the AIAA/ASME/ASCE/AHS/ASC Structures, Structural Dynamics and Material Conference (American Institute of Aeronautical and Astronautics, Washington, DC, 1992), pp. 566–576.
[7] J. P. Maillard and C. R. Fuller, ''Advanced time and wave-number sensing for structural acoustic systems. I. Theory and design,'' J. Acoust. Soc. Am. **95**, 3252–3261 (1994).
[8] F. Fahy, *Sound and Structural Vibration: Radiation, Transmission and Response* (Academic, New York, 1985), p. 76.
[9] P. M. Morse and K. U. Ingard, *Theoretical Acoustics* (Princeton U. P., Princeton, NJ, 1968), p. 185.
[10] M. D. Greenberg, *Foundations of Applied Mathematics* (Prentice-Hall, Englewood Cliffs, NJ), p. 102.
[11] F. J. Harris, ''On the use of windows for harmonic analysis with the discrete fourier transform,'' Proc. IEEE **66**, 51–83 (1978).
[12] M. S. Anderson and E. F. Crawley, ''Discrete Shaped Strain Sensors for Intelligent Structures,'' Proceedings of the AIAA/ASME/ASCE/AHS/ASC Structures, Structural Dynamics and Material Conference (American Institute of Aeronautics and Astronautics, Washington, DC, 1990), p. 567.
[13] W. H. Press, B. P. Flannery, S. A. Teukolsky, and W. T. Vetterling, *Numerical Recipes in C: The Art of Scientific Computing* (Cambridge U. P., New York, 1988), p. 114.